

Chapter 2

Translational Photoacoustic Microscopy

Yong Zhou and Lihong V. Wang

Abstract Photoacoustic microscopy (PAM), combining the advantages of optical excitation and of acoustic detection, has been widely used for both structural and functional imaging with scalable resolution and penetration in biological tissues. In this chapter, we provide a detailed discussion on PAM in translational studies. We first summarize the principles and major implementations of this technology. Then we introduce the state of the art in translational PAM, including studies on burns, peripheral arterial occlusive disease, eye disease, diabetic microvascular complications, pain, melanoma, gastrointestinal tract disease, and the brain. Finally, we discuss the major challenges and future directions of translational PAM.

1 Introduction

Imaging modalities, including positron emission tomography (PET), X-ray computed tomography (X-CT), magnetic resonance imaging (MRI), and ultrasound (US), have greatly facilitated diagnosis and treatment in clinics. Each modality, however, involves trade-offs. In addition to their high cost, PET and X-CT employ ionizing radiation, which is potentially carcinogenic. Thus, how to decrease their radiation dose while keeping high image quality has attracted increasing attention. MRI is time-consuming and even more costly, hindering its wide routine usage. In addition, because of the high magnetic and electrical fields, patients with implants are not recommended for MRI imaging. US is relatively cheap and easy to operate. Because of the strong acoustic reflectance at the tissue surface, it has been extremely powerful in fetus imaging. However, the contrast inside soft tissue is low.

Y. Zhou · L.V. Wang (✉)

Optical Imaging Laboratory, Department of Biomedical Engineering, Washington University
in St. Louis, St. Louis, MO 63130, USA
e-mail: lhwang@wustl.edu

Nevertheless, all of these imaging modalities, although their contrasts are different, share the same advantage—deep penetration, which is one of the most fundamental requirements for clinical applications.

With high resolution and contrast, optical microscopy has been widely used in a number of fields, especially in basic sciences. However, it has been clinically limited because of its shallow imaging depth in tissue. When light travels into tissue, its effective focusing ability degrades quickly because tissue is highly scattering [1]. Two optical regimes can be classified based on the number of scattering events: ballistic (minimally scattered) and diffusive (multi-scattered). In the ballistic regime (~ 1 mm in tissue), optical microscopy provides high resolution, but the penetration is insufficient for many human applications. On the contrary, in the diffusive regime, diffuse optical tomography provides macroscopic imaging with centimeters of penetration but lacks spatial resolution—roughly one-third of the depth [2]. Achieving deep penetration with high resolution remains a challenge for pure optical imaging.

Combining optical excitation and ultrasonic detection, photoacoustic tomography (PAT) offers deep imaging with high resolution [3–6]. With optical excitation, PAT maintains the high contrast of optical imaging. Because of the low scattering of ultrasonic waves in tissue, PAT achieves high spatial resolution at depth. Several advantages make PAT suitable for clinical application. First, it can image deep: up to 7 cm deep images have been reported with a spatial resolution of a few hundred micrometers [3]. Second, it detects a rich variety of optical absorbers, both exogenous (e.g., methylene blue) and endogenous. So far, many endogenous contrasts have been imaged with high sensitivity, such as hemoglobin [7], myoglobin [8], DNA and RNA [9], water [10], lipid [11], cytochrome c [12], bilirubin [13], melanin [14, 15], and methemoglobin [16]. Third, similar to US imaging, PAT has scalable resolution. Thus, both fine structures (such as organelles) and global features (such as organs) can be detected with the same contrast [17–21]. Fourth, because different chemical compositions have different absorptions, features can be distinguished by multi-wavelength imaging. For example, *in vivo* human nevi and their surrounding vasculature have been successfully differentiated by PAT [21]. Fifth, because hemoglobin is confined within blood vessels, vasculature can be imaged with high contrast-to-noise ratio. With these advantages, PAT has become a promising translational technique for medical diagnosis. To date, PAT has been widely applied to studies in a variety of fields, including dermatology [22], ophthalmology [23], oncology [24], gastroenterology [25], and neuroscience [3].

Based on different image reconstruction mechanisms, PAT can be further divided into two embodiments: raster-scanning-based photoacoustic microscopy (PAM) and reconstruction-algorithm-based photoacoustic computed tomography (PACT) [5, 6, 26, 27]. In this chapter, we will introduce the state of the art in PAM for clinical applications. A detailed description of PACT can be found in another chapter of this book. Below, we first introduce the basic principles of PAM and its major implementations. Then we discuss the main translational applications of PAM, including the detection and study of burns, peripheral arterial occlusive disease, eye disease, diabetic microvascular complications, pain, melanoma,

gastrointestinal tract disease, and the brain. Finally, we summarize the field of translational PAM, point out new potential applications, discuss the major challenges, and project the future.

2 Principle and Major Implementations of Photoacoustic Microscopy

2.1 Fundamental Principles

PAM, based on the photoacoustic effect, is a cross-sectional or three-dimensional (3D) imaging modality. In PAM, normally a short-pulsed laser illuminates the object. To achieve higher conversion efficiency, the laser pulse should be shorter than both the thermal relaxation time and stress relaxation time [1]. The absorption of light will generate an initial temperature rise, which subsequently is converted to a pressure rise via thermoelastic expansion. The pressure rise propagates as a photoacoustic wave and is finally detected by an ultrasonic transducer to form a high resolution image of the absorption sources. Each laser pulse generates a one-dimensional depth-resolved image. Usually two-dimensional raster scanning is adopted to form a three-dimensional image. Although a pulsed laser is the most commonly used illumination source, an intensity-modulated continuous-wave light source can be used alternatively, with degraded excitation efficiency [28].

In PAM, the axial resolution is estimated by $0.88c/\Delta f$ [29, 30], where c is the speed of sound in soft tissue, and Δf is the frequency bandwidth of the ultrasonic transducer. While c is basically constant in soft tissue (around 1500 m/s), Δf becomes the primary factor determining the system's axial resolution. Based on the limiting factor for lateral resolution, PAM can be further divided into optical-resolution PAM (OR-PAM) [26] and acoustic-resolution PAM (AR-PAM) [27]. In OR-PAM, the optical focus—much tighter than the acoustic focus—provides a high lateral resolution, given by $0.51\lambda/NA$, where λ is the light wavelength, and NA is the numerical aperture of the optical objective [17]. In AR-PAM, the acoustic focus is tighter than the optical focus. The lateral resolution in AR-PAM is given by $0.72\lambda/NA$, where λ is the central acoustic wavelength of the ultrasonic transducer, and NA is the numerical aperture of the ultrasonic transducer [31]. The coefficients differ in the lateral resolution expressions (i.e., 0.51 vs. 0.72), because optical excitation is based on light intensity, while ultrasonic detection is based on acoustic amplitude.

Taking advantage of tight optical focusing, OR-PAM enables fine lateral resolution ranging from a few hundred nanometers to a few micrometers [17, 32]. So far, by using OR-PAM, single organelles (such as cell nuclei and mitochondria) and single cells (such as red blood cells and melanoma cells) have been successfully imaged [9, 12, 14, 19]. In addition, OR-PAM has also been widely applied to functional studies in vivo by imaging blood flow and oxygen saturation [33–36]. However, working in the ballistic regime, the imaging depth is confined to the

optical diffusion limit [37, 38]. Because acoustic scattering is much lower than the optical scattering, acoustic focusing can be better maintained at depth. Thus, AR-PAM can break the optical diffusion limit and work up to a few millimeters deep [39]. To achieve high lateral resolution, a high frequency ultrasonic transducer is desired; however, higher frequency acoustic waves suffer from higher propagation loss, and the penetration depth is limited. Thus, there is a trade-off between resolution and penetration in AR-PAM. Using a 50 MHz transducer, AR-PAM has shown great success in human microvasculature imaging in the skin *in vivo*, with a lateral resolution of around 45 μm and a penetration of 1.48 mm [5, 21].

2.2 Major Implementations

Figure 1 shows a typical OR-PAM system [19]. To measure tissue oxygen saturation, a laser system with dual wavelengths (e.g., 532 and 559 nm) is used. After being reshaped by an iris, focused by a convex lens, and filtered by a pinhole, the light beam is coupled into a single-mode optical fiber. A neutral-density filter in front of the optical fiber coupler controls the incident pulse energy. The output of the optical fiber is first collimated by an objective, and then reflected by a mirror. A second objective focuses the beam into the target. To monitor the laser energy fluctuation for image compensation, a beam sampler is placed before the mirror to reflect some light to a photodiode. An optical and acoustic beam combiner, including a right-angle prism and rhomboid prism, confocally aligns the optical and acoustic foci. A silicone oil layer, filling the gap between the right-angle prism and the rhomboid prism, transmits light and reflects ultrasound. To collimate the

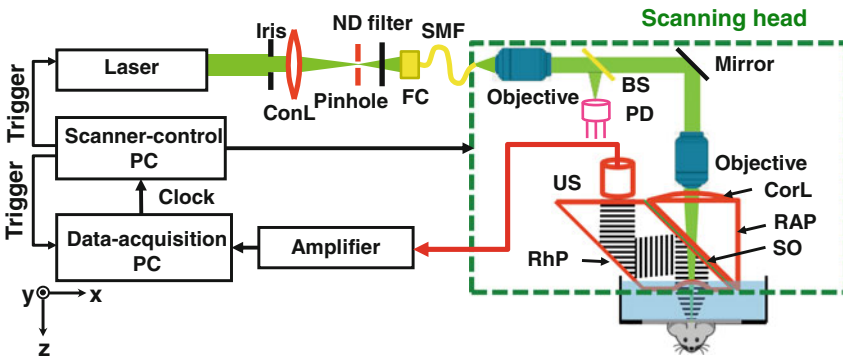


Fig. 1 Typical OR-PAM system, where the scanning head is framed with *dashed lines*. *BS* beam sampler; *ConL* condenser lens; *CorL* correction lens; *FC* fiber coupler; *ND* filter, neutral density filter; *PD* photodiode; *RAP* right angle prism; *RhP* rhomboid prism; *SO* silicone oil; *US* ultrasonic transducer

ultrasound wave, an acoustic lens is usually attached below the rhomboid prism, and a flat high-frequency ultrasonic transducer is placed above the rhomboid prism for detection. An optical lens attached to the top surface of the right-angle prism for wavefront correction enables diffraction-limited optical resolution. The rhomboid prism reflects the ultrasonic signals twice to convert the intermediate shear wave back into a longitudinal component, which maximizes the detection sensitivity because the ultrasonic transducer is much more sensitive to longitudinal acoustic waves than to shear waves. Each laser pulse generates a one-dimensional image (A-line), and two-dimensional transverse scanning of the PAM head forms the final three-dimensional image.

Figure 2 shows a typical AR-PAM system [5]. A short-pulsed wavelength-tunable laser is used as the illumination source. Different from OR-PAM, AR-PAM uses a multi-mode optical fiber to couple the laser beam into the scanning head. To form dark-field illumination, a conical lens and a mirror are used. A flat ultrasonic transducer attached to an acoustic lens detects the PA signals. As in OR-PAM, each laser pulse generates a one-dimensional image (A-line), and two-dimensional transverse scanning of the head forms the final three-dimensional image.

As shown in Figs. 1 and 2, OR-PAM and AR-PAM differ as follows. **(i) Pulse energy.** Since optical focusing is tight in OR-PAM, the pulse energy required to provide a high signal-to-noise ratio (SNR) is smaller—a few hundred nano-joules in in vivo imaging. To achieve similar optical fluence, AR-PAM requires much higher pulse energy: usually at least a few hundred micro-joules. **(ii) Laser repetition rate.** Because the limited average laser power presents a trade-off between laser pulse energy and repetition rate, a high repetition rate laser is usually employed in OR-PAM (e.g., tens to hundreds of kHz) to improve the imaging speed, while a relatively low repetition rate laser (e.g., a few kHz) is used in AR-PAM to meet the

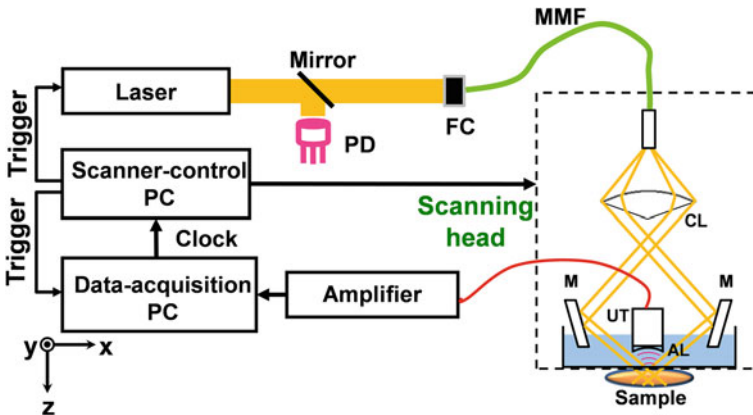


Fig. 2 Typical AR-PAM system, where the scanning head is framed with dashed lines. AL acoustic lens; CL conical lens; FC fiber coupler; M mirror; MMF multi-mode fiber; PD photodiode

pulse energy requirement. **(iii) Laser wavelength.** Because OR-PAM works in the shallow ballistic regime, for vasculature imaging, wavelengths where blood has high absorption, such as 532 nm, are used. For deep vasculature imaging with AR-PAM, longer wavelengths are typically used, such as 650 nm, where light suffers less attenuation in tissue than at 532 nm. **(iv) Spatial filtering of the laser beam.** To achieve optical diffraction-limited resolution, spatial filtering with a lens and a pin-hole is required in OR-PAM. By contrast, in AR-PAM, because the lateral resolutions are defined acoustically, light does not need to be tightly focused, and thus spatial filtering is not needed. A related difference is that a single-mode fiber is used in OR-PAM to ensure the optical resolution, while a multi-mode fiber is used in AR-PAM to maximize the incident optical energy. **(v) Illumination pattern.** Because of the high incident pulse energy in AR-PAM, dark field illumination is preferred to minimize the signals from the skin surface. On the other hand, bright field illumination is used in OR-PAM. **(vi) Ultrasonic transducer.** A high-frequency transducer (e.g., 50 MHz) is used in OR-PAM to achieve high axial resolution and high detection sensitivity. On the contrary, for deep imaging, ultrasonic transducers with a lower central frequency (e.g., 20 MHz) are used in AR-PAM, because high frequency acoustic signals suffer from more attenuation in tissue. **(vii) Data acquisition (DAQ).** A high laser repetition rate generates a large amount of data in a fixed time (i.e., per second). Thus, a DAQ with fast data transfer rate is required in OR-PAM, and a relatively slow one suffices in AR-PAM. These features of typical OR- and AR-PAM are compared in Table 1.

On the other hand, OR-PAM and AR-PAM also share some common features. **(i) Laser pulse duration.** To satisfy the thermal and stress requirements and to increase the excitation efficiency, usually the pulse duration is just a few nano-seconds in both AR- and OR-PAM. **(ii) Wavelengths.** They both require dual wavelength for oxygen saturation (sO_2) detection. **(iii) Ultrasonic transducer.** To achieve high sensitivity, typically they both use focused ultrasonic transducers. In addition, the dual foci in both OR- and AR-PAM are configured confocally to maximize the system sensitivity. **(iv) Axial resolution.** The axial resolution in both OR- and AR-PAM is determined by the bandwidth of the transducer.

In summary, because AR-PAM can break the optical diffusion limit and achieve deep imaging, it has been more commonly applied in human studies than OR-PAM.

Table 1 Comparison of typical OR- and AR-PAM

	OR-PAM	AR-PAM
Typical pulse energy	Low	High
Laser repetition rate	High	Low
Laser wavelength	Short	Long
Spatial filtering of the laser beam	Yes	No
Illumination pattern	Bright field	Dark field
Ultrasonic transducer	High frequency	Low frequency
DAQ	Fast	Slow

However, for some targets, such as finger cuticle microvasculature, OR-PAM has advantages for in vivo human imaging. In the following sections, we will present the capabilities of both AR- and OR-PAM in human imaging and clinical applications.

3 Translational Research of Photoacoustic Microscopy

3.1 Burn Imaging

A burn is characterized by both its extent and depth. Based on different depths, burns can be further divided into superficial, partial-thickness, and full-thickness burns. While clinical assessment of the burn depth in superficial and full-thickness burns is generally accurate, partial-thickness burn depth measurements are frequently inaccurate. Because there are increased blood contents (increased optical absorption) around the burn boundaries, PAM can image burns with high contrast [22, 40, 41].

Acute thermal burns were induced in vivo on pig skin by heating at 175 °C for 20 s. A photograph of the skin burn is shown in Fig. 3a. After excision of the skin with burns, a volume of $10 \times 10 \times 3 \text{ mm}^3$ was imaged by PAM. A two-dimensional MAP image is shown in Fig. 3b, where the hyperemic ring structure can be clearly identified and agrees well with the photograph. The PA amplitude ratios of the

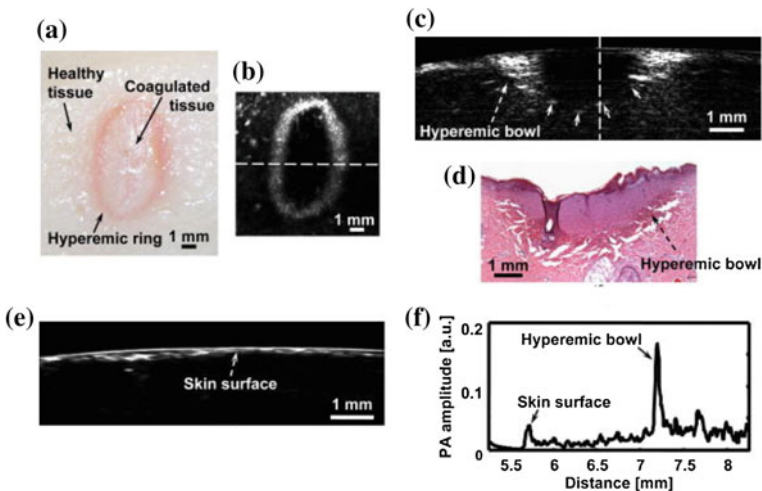


Fig. 3 AR-PAM of burn. **a** Skin burn photograph. **b** Photoacoustic MAP image of the burn. Photoacoustic B-scan (**c**) and corresponding histology image (**d**) of the burn. **e** Photoacoustic image of healthy subject. **f** Depth profile along the *dashed line* in (**c**) (Figure reproduced with permission from [22])

hyperemic ring to the inner coagulated tissue and to the outer normal tissue were 20.4 and 9.5, respectively. The high amplitude ratios provided high contrast to identify the extent of the burn. The depth profile of the burn is shown in Fig. 3c, where the hyperemic bowl is clearly seen and agrees well with the histological photograph (Fig. 3d). A typical B-scan image of healthy skin is shown in Fig. 3e, showing no hyperemic bowl structure. To determine the depth of the burn, a representative depth profile within the B-scan image is shown in Fig. 3f. The two peaks correspond to the skin surface and inner boundary of the hyperemic bowl. Thus, the depth of the burn was measured to be 1.73 mm.

3.2 *Peripheral Arterial Occlusive Disease Detection*

Peripheral arterial occlusive disease (PAOD) refers to the obstruction of large arteries outside the brain, coronary, and aortic arch vasculature [42]. Causes of PAOD include hypertension, atherosclerosis, and diabetes mellitus. One way to diagnose PAOD is by momentarily occluding the upstream blood flow in large arteries. When the occlusion is removed, the reactive hyperemia in healthy subjects is obvious (around ten times the value during the resting state) but it is significantly reduced in subjects with PAOD. In addition, the recovery from hyperemia to the resting condition is prolonged in patients with PAOD [43].

In one study, the microvascular structure from the palm of a healthy volunteer was imaged at 570 nm, as shown in Fig. 4a [44]. The B-scan images before, during, and after occlusion are shown in Fig. 4b, c, and d, respectively. From those images, a significant reduction of signal strength can be observed during occlusion, while a drastic increase of signal strength appears after occlusion. Since the PA signal is proportional to the local blood perfusion, the ischemia and hyperemia processes are clearly distinguished.

To quantitatively describe the difference between healthy subjects and patients with PAOD during the occlusion, a model has been developed in the literature [45]:

$$I(t) = I_r[1 - \exp(-t/\tau_1)] \times [1 + (\rho_m - 1) \times \exp(-t/\tau_2)],$$

where $I(t)$ and I_r are the time-dependent and resting-state blood flows, respectively; t is the time; τ_1 and τ_2 are decay constants for arteriole and capillary vessels, respectively; and ρ_m is the ratio of the maximum perfusion during hyperemia to the normal resting condition. Based on the assumption that the temporal change in blood volume is proportional to the temporal change in blood flow, our PA measurement should also fit with this model. Using the reported time constants for healthy subjects, a quantitative analysis of the blood volume change is shown in Fig. 5. It clearly illustrates that our PA measurements agree well with the model, with R^2 values of 0.92 and 0.95 for two successive ischemic events.

These results indicate that AR-PAM can be used to assess microvascular functionality in healthy volunteers. Specifically, the ischemic and hyperemic process

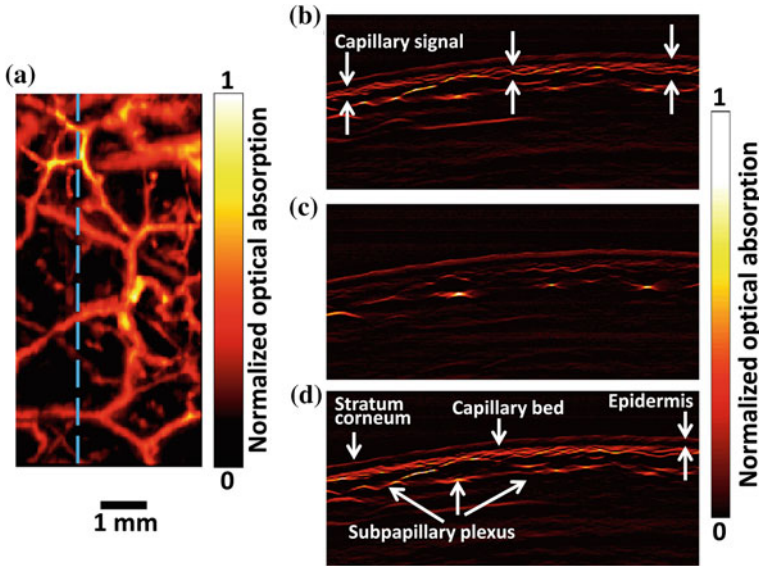


Fig. 4 **a** Maximum-amplitude-projection image taken from the palm of a healthy volunteer. The *blue dashed line* indicates the cross-section selected for functional analysis. **b** B-scan image of the monitored cross-section before blood flow was occluded. **c** B-scan image during the occlusion. **d** B-scan image acquired after the occlusion. The scale bar applies to all panels (Figure reprinted with permission from [44])

during and after occlusion of large vessels are successfully detected by AR-PAM. The next step is to apply AR-PAM in patient studies, including patients with hypertension and diabetes. Significant differences between patients and healthy people are expected. Thus, we believe that AR-PAM can be a useful tool for clinical characterization of the microcirculation and can aid in microvasculature-related disease diagnosis.

3.3 Eye Imaging

Due to an increase in the aging population, the number of people with visual impairment has been significantly growing. Although eye diseases can be divided into different categories, most of them are manifest in the ocular microcirculation. By the virtue of the transparency of the eye, high resolution ocular imaging has been achieved, including fluorescence angiography [46] and optical coherence tomography [47]. With a high sensitivity in imaging microvasculature, label-free photoacoustic ophthalmic angiography has also been developed.

Recently, both AR-PAM and OR-PAM have been applied for eye imaging [23, 48–51]. A rabbit eye *in vivo* was imaged by AR-PAM [48], and both the

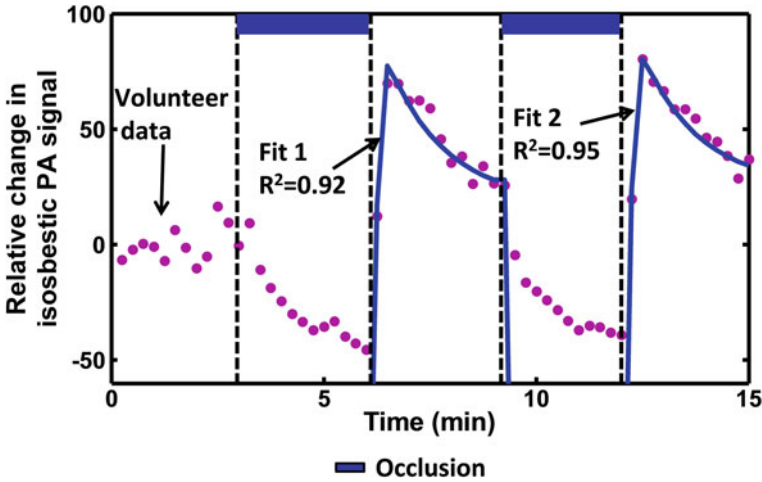


Fig. 5 Relative change in the photoacoustic signal during multiple occlusions. Changes in the photoacoustic signal correspond to changes in the total amount of blood in the vessel. During the occlusion (*blue boxes*), the amount of blood decreases; immediately following the occlusion, the vessels enter the hyperemic state. *Dots* experiment data; *curve* model fitting (Figure reprinted with permission from [44])

anterior segment structures, such as the cornea, and the posterior segment structures, such as the retina and choroid, were detected simultaneously, as shown in Fig. 6a. The anterior segment (iris vasculature) [50] and posterior segment (retina vasculature) [23] have also been imaged by OR-PAM, as shown in Fig. 6b and c, respectively. Compared to AR-PAM, OR-PAM has optically defined resolution; thus, fine microvascular structures can be visualized. In addition, oxygen saturation was also detected by using dual wavelengths (570 and 578 nm), as shown in Fig. 6b. Note that the laser pulse energy density in both AR-PAM and OR-PAM are well within the American National Standards Institute (ANSI) safety limits for eye

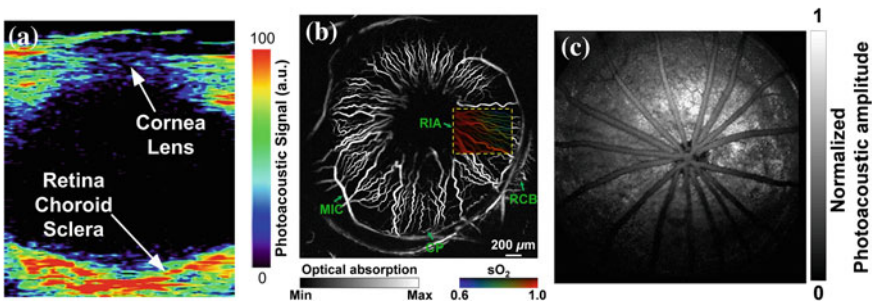


Fig. 6 Photoacoustic microscopy of the eye. **a** AR-PAM of a rabbit eye. OR-PAM of the anterior segment (**b**) and posterior segment (**c**) (Figures reprinted with permission from [48, 50, 52])

exposure because of the high absorption of hemoglobin and high sensitivity of PAM to absorption.

Since the eye is almost transparent, light can be effectively focused into it. Consequently, high optical resolution imaging, such as OCT, can be performed. With the same focusing mechanism, OR-PAM should also be able to achieve high resolution eye imaging in humans *in vivo*. Recall that AR-PAM does not require optical focus. Since acoustic scattering in the eye is also low, acoustic focusing can be maintained, as shown Fig. 6a. Thus, AR-PAM also should be able to achieve eye microvasculature imaging. In sum, although photoacoustic ophthalmic imaging has not been applied in humans yet, there are no apparent fundamental obstacles.

3.4 Diabetic Microvasculature Complication Study

Diabetes, defined by an elevated glucose level in the blood stream, is one of the most common diseases. It is estimated that worldwide there are about 382 million people with diabetes in 2013, and the number will increase to 592 million by 2035 [53]. The major complications of diabetes are related to damage of the blood vessels at both macrovascular and microvascular scales [54]. Macrovascular diseases include coronary artery disease, stroke, and peripheral vascular disease, while microvascular complications mainly include damage to the eyes, nerves, and kidneys [55].

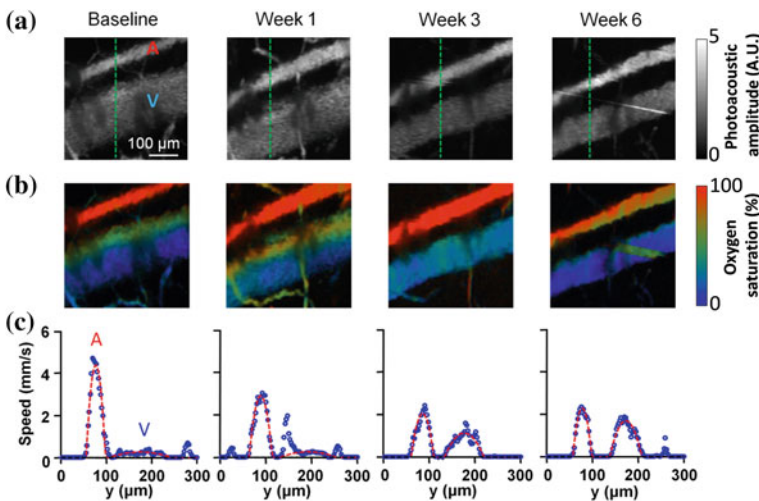


Fig. 7 Longitudinal monitoring of a vessel pair in a streptozotocin mouse showing changes in structure (a), oxygen saturation (b), and flow velocity (c). A artery; V vein (Figure reprinted with permission from [56])

With high spatiotemporal resolution, OR-PAM has recently been used for early detection of microvascular morbidity in diabetes [56]. A streptozotocin (STZ) mouse model was used, and the blood glucose level was monitored by a glucometer. Multiple parameters in an artery and vein pair in the ear were monitored before and after administration of STZ, including vessel diameter, oxygen saturation (sO_2), blood flow speed, and total hemoglobin concentration (HbT). After the administration of STZ, six mice were imaged once a week for 6 weeks to observe the changes of those vascular parameters. Figure 7 shows a representative result of one STZ-induced mouse, where the diameter, HbT, sO_2 , and flow speed were longitudinally monitored. The same measurement procedure was applied for all six mice, and the results for all the mice are summarized in Fig. 8. It is clear that with the increase of blood glucose (Fig. 8a), the diameter of both the artery and vein decreased, especially in the vein (Fig. 8b), which has been explained by compensation for volume loss because of polyurea. The polyurea was also responsible for the initial body weight loss shown in the Fig. 8c. As shown in Fig. 8d and e, there were no obvious sO_2 and HbT changes. Another significant change was the flow speed (Fig. 8f), which can be explained as follows. Since the same flux of oxygen and nutrients need to be maintained, the volumetric flow rate must be kept constant. If the vessel diameters decreased, the flow speed in artery and vein had to increase accordingly. The oxygen extraction fraction (OEF) and metabolic rate of oxygen (MRO_2) were also calculated, but no significant changes were observed, as shown in Fig. 8g and i, respectively. In sum, the result showed two important parameters, vessel diameter and blood flow speed, had significant changes in the development

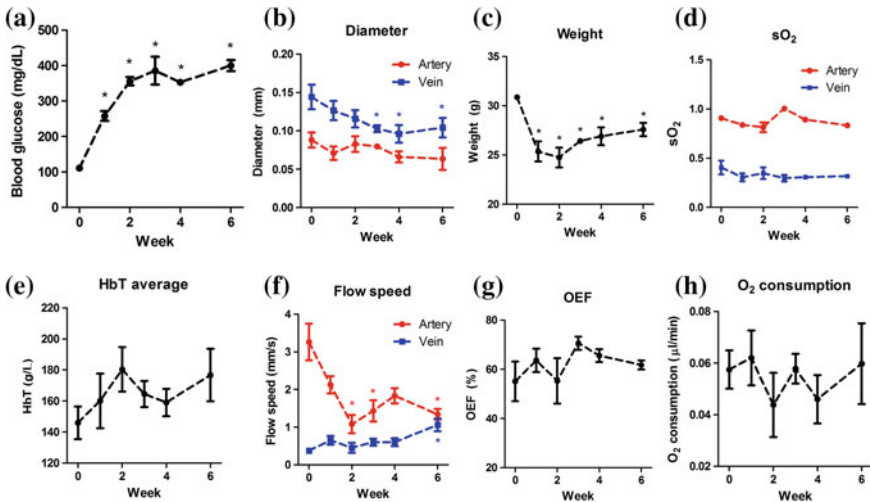


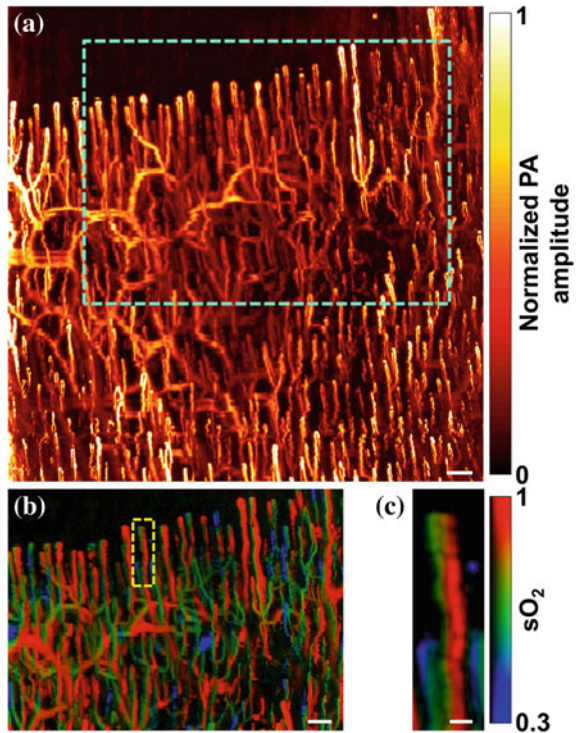
Fig. 8 Statistics of all mice monitored for 6 weeks, including blood glucose level (a), vessel diameter (b), total body weight (c), oxygen saturation (d), total hemoglobin (e), flow speed (f), oxygen extraction fraction (g), and oxygen consumption (h). *HbT* total hemoglobin; *OEF* oxygen extraction fraction; *sO₂* oxygen saturation (Figure reproduced with permission from [56])

of diabetes. Thus, OR-PAM can be used for monitoring vascular complications of diabetes in mice *in vivo*.

Although OR-PAM has been used to image microvasculature in mice ever since it was invented, it has not been applied to human imaging due to the thickness of human skin. Very recently, the first human image was acquired by Hu et al. [7]. The human finger cuticle microvasculature was successfully visualized *in vivo*, as shown in Fig. 9. Individual capillary loops were clearly identified (Fig. 9a), and the sO_2 within these loops was revealed with dual wavelength detection (Fig. 9b). It is clear that the greatest gradient of sO_2 in the loop occurred at the tip, indicating the biggest oxygen release from the blood (Fig. 9c).

In principle, OR-PAM can detect the same microvascular parameters—including vessel diameter, blood flow speed, HbT, and sO_2 —in human finger cuticles as in mice. Thus, we anticipate that diabetes-induced microvascular complications can also be detected in humans *in vivo* by OR-PAM. With its high spatiotemporal resolution and spectral decomposition ability, OR-PAM is a promising tool for clinical diagnosis of diabetes microvascular complications in the early stages.

Fig. 9 OR-PAM of human cuticle. **a** Structural image. **b** Oxygen saturation (sO_2) map in the *dashed box* region in (a). **c** The capillary loop indicated in (b). Scale bars in (a) and (b) are 200 μm . Scale bar in (c) is 50 μm (Figure reprinted with permission from [7])



3.5 Pain Study

Complex regional pain syndrome (CRPS) is a chronic systemic disorder characterized by disproportionate pain and autonomic changes. Among all the causative factors, vascular and microcirculatory dysfunction play important roles in the pathogenesis of this disabling syndrome [57]. It has been pointed out that, because of the connection between the microvascular blood supply and the development of neuropathic pain, microcirculatory parameters including the rate and volume of blood flow and tissue oxygen saturation (sO_2), may potentially be used to diagnose CRPS and to indicate the activity of the disease [58].

PAM is potentially an ideal tool for monitoring and diagnosing CRPS by imaging peripheral blood perfusion. Recently, by combining of OR- and AR-PAM, microcirculatory changes in patients with CRPS type I were identified after stellate ganglion blocks (SGB) [59]. For each patient, two sites of the same hand were imaged: superficial microvasculature at the cuticle by OR-PAM, and deeper and larger vessels at the back of the hand by AR-PAM, as shown in Fig. 10a. During the experiments, the distance between the patient's hand and the ultrasonic transducer was fixed for fair comparison. Skin temperature in the block side increased 1.1 ± 0.1 °C 10 min after SGB. Meanwhile, the pain level reduced by 2.5 ± 0.6 on discharge.

In AR-PAM, signals down to 1 mm deep were collected. Signals at different depths were distinguished based on the high axial resolution of AR-PAM, as shown in Fig. 10b–e. It is clear that there are more blood vessels visible and stronger signals after SGB. Since the photoacoustic signals are proportional to the local optical fluence and absorption coefficient of the target, stronger photoacoustic signals correspond to a greater absorption coefficient if the optical fluence is kept constant [60]. Thus, after the block, there was probably an increase in blood

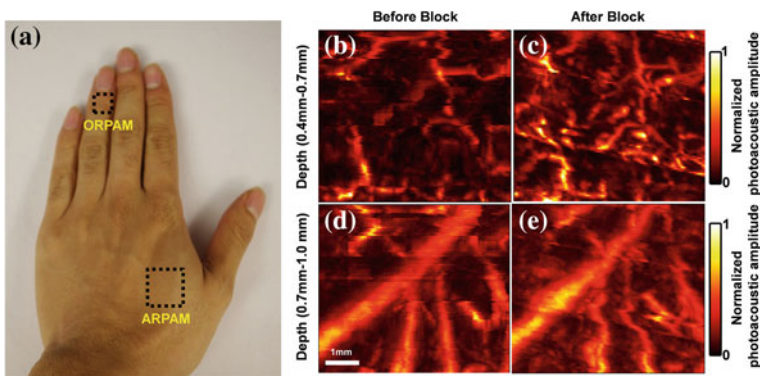


Fig. 10 a Regions scanned in OR- and AR-PAM. Maximum amplitude projection (MAP) images of vasculature in the back of one patient's hand by AR-PAM in the depth range between 0.4 and 0.7 mm, before block (b) and after block (c). MAP images in the depth range between 0.7 and 1 mm, before block (d) and after block (e) (Figure reprinted with permission from [59])

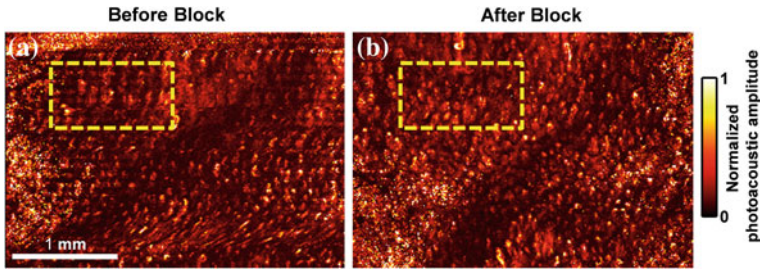


Fig. 11 OR-PAM vasculature image of the fingertip of one patient. Maximum-amplitude-projection image of scanned region before block (a) and after block (b). The *dashed box* represents the region used for statistical analysis. (Figure reprinted with permission from [59])

perfusion. As shown in Fig. 11, the photoacoustic signals in finger cuticle images acquired by OR-PAM also increased after the block, which is consistent with the results from AR-PAM.

Statistical analysis of all the patients' data is shown in the Fig. 12. Figure 12a shows the average increase in signal intensity at different depths measured by AR-PAM after the block. On average, there was $>50\%$ signal increase in all depth ranges. Similar results can also be found from the OR-PAM measurement, as shown in Fig. 12b. Based on the dual-wavelength measurement by AR-PAM, the average sO_2 increased by around 4 %, as shown in Fig. 12c.

In sum, microvasculature changes were successfully detected by PAM in patients. Between pre- and post-SGB, there was about a 50 % increase in signal intensity in PAM and a 4 % increase in sO_2 , which agreed with the increased temperature and decreased pain level. The results showed blood perfusion increased after SGB, which was consistent with prior reports. In these preliminary results, PAM showed its potential in helping monitor and diagnose CRPS.

3.6 Melanoma Detection

Melanoma, the most deadly form of skin cancer, is now the fifth most common cancer in the United States [61]. In addition, the incidence of melanoma is increasing faster than that of any other cancer [62]. Surgical removal of the melanoma is the standard of treatment, and tumor thickness is the key tumor characteristic. However, tumor thickness is currently measured by biopsy, but the true tumor depth may not be determined because usually only part of the tumor is sampled. Thus, an *in vivo* complete measurement of tumor depth is desired. High-resolution PAM suggests itself here because the melanin in melanomas has a very broad and strong absorption spectrum.

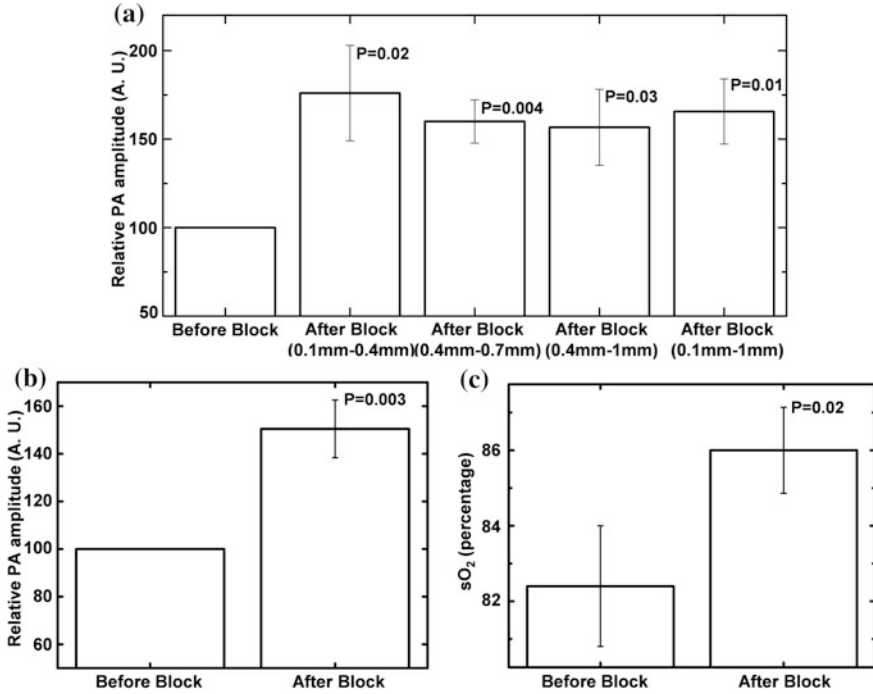


Fig. 12 **a** Normalized photoacoustic (PA) signal measured by AR-PAM before and after block in different depth ranges. **b** Normalized PA signal measured by OR-PAM before and after block. **c** Average sO₂ measured by AR-PAM before and after block (Figure reprinted with permission from [59])

Recently, a handheld PAM system for melanoma depth detection was reported [24], and is shown in Fig. 13. Compared with a typical AR-PAM system, there are two advantages to this handheld system. First, the light delivery bypasses the tumor instead of going through it. Thus, more light reaches the bottom boundary of the melanoma. Second, the handheld design makes this system quite suitable for clinical application.

Phantom experiments were conducted to demonstrate the ability of the handheld probe to measure deep melanomas. Different diameters (7, 9, and 14 mm) of melanoma phantoms were prepared with varied thicknesses. As shown in Fig. 14a–c, both the top and bottom boundaries of all the melanoma phantoms were successfully detected, with maximum and minimum thicknesses of 4.1 and 0.7 mm, respectively. Therefore, melanoma phantoms with all the tumor classifications in the staging system were measured. As shown in Fig. 14d, all the measured thicknesses agree well with the preset values.

Figure 15 shows the in vivo experimental results from the handheld probe. Both the top and the bottom boundaries of the melanoma and the skin surface can be clearly seen (Fig. 15a). The tumor thickness was measured 3.66 mm (Fig. 15b),

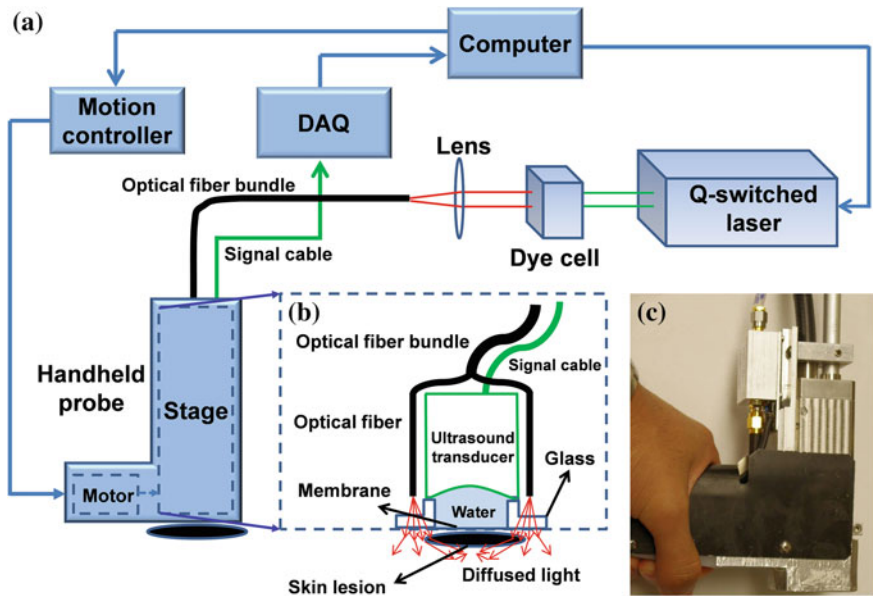


Fig. 13 Experimental handheld PAM melanoma measurement system. **a** A schematic of the system. **b** Components inside the translation stage of the handheld probe. **c** Photograph of the handheld probe (Figure reprinted with permission from [24])

which is accordance with the real melanoma thickness (Fig. 15c). With high accuracy in melanoma depth detection, this system is ready to be clinically applied on melanoma patients.

3.7 Gastrointestinal Tract Disease Detection

Compared to pure optical or ultrasonic endoscopy, photoacoustic endoscopy (PAE) is more challenging because it requires both optical excitation and acoustic detection. However, because it can provide both high optical contrast and deep acoustic penetration, it has been drawing more and more attention. Recently, exciting advances have been achieved, especially in gastrointestinal tract (GI) imaging [25, 63–65].

From the resolution point of view, most of the reported photoacoustic endoscopy falls into AR-PAM category. Therefore, anatomic structures can be imaged at depths. Figure 16 shows representative PAE B-scan images of a rabbit esophagus (upper GI tract), with a 160° angular field of view and 5.4 mm depth. Several landmarks can be clearly identified, including the esophageal wall, the surface of a neighboring organ, and blood vessels in the mediastinum. The lower GI tract has also been imaged by PAE, with typical images shown in Fig. 17. While ultrasound

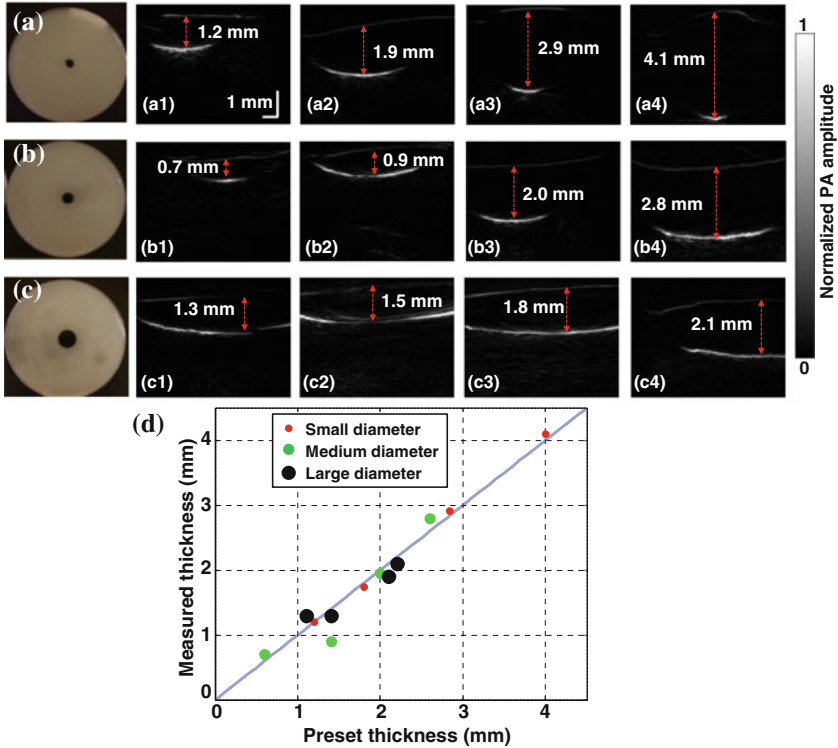


Fig. 14 Handheld PAM of melanoma phantoms. Photos of melanoma phantoms with different diameters, **a** 7 mm; **b** 9.5 mm, and **c** 14 mm. (a1–a4), (b1–b4), and (c1–c4): PAM images of different thicknesses of melanoma phantoms with the same diameter as in (a), (b), and (c), respectively. **d** Measured thicknesses of melanoma phantoms versus preset thicknesses. (Figure reprinted with permission from [24])

clearly shows the spine structure, PAE detects microvasculature in the colorectum and adjacent organs with high sensitivity. Note that blood vessels as deep as 6 mm can still be measured by PAE. These systems are now ready for imaging human GI tracts. Another important direction for PAE is urogenital disease diagnoses, including endometrial, cervical, and prostate cancers.

3.8 Brain Study

Understanding how our brains work is one of the most exciting research areas. With high spatial resolution, human brain imaging is one of the most powerful media in brain research. Although a myriad of bits and pieces from studies of the brain has

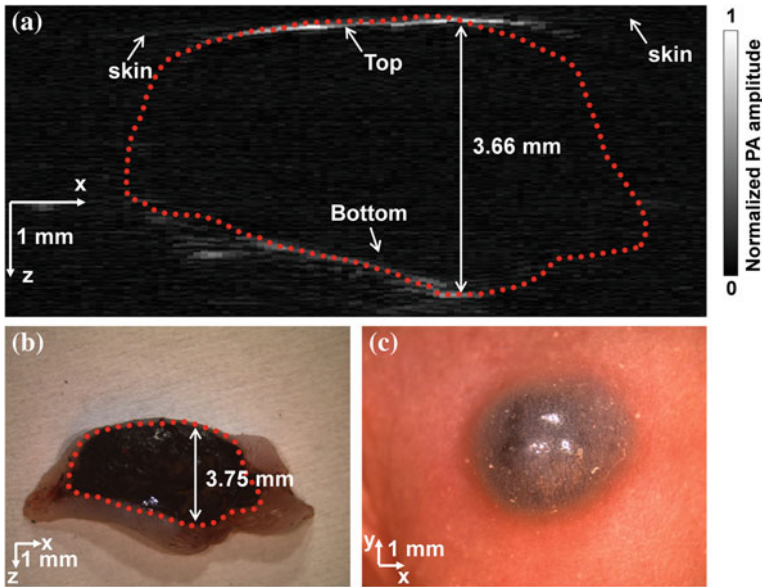


Fig. 15 Handheld PAM of melanoma in a nude mouse in vivo. **a** PAM image clearly showing both the *top* and *bottom* boundaries of the melanoma and the skin surface. The *red dots* outline the melanoma according to the shape of the excised melanoma (*red dots*) in its photograph **(b)**. Photograph of the melanoma taken in vivo **(c)** (Figure reproduced with permission from [24])

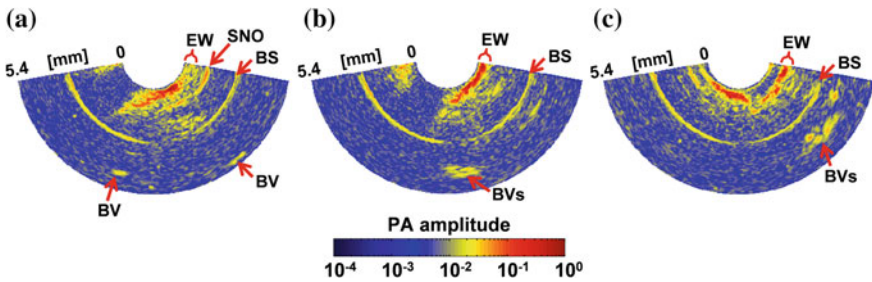


Fig. 16 Three representative photoacoustic endoscopy images of a rabbit esophagus in vivo. The *left* and *lower* portion of each image correspond to the left and the dorsal side of the animal, respectively. *BS* bounceback signals; *BV* blood vessels; *EW* esophageal wall; *SNO* surface of a neighboring organ (Figure reprinted with permission from [63])

been gathered in the last few decades, we still fall far short of a comprehensive understanding of brain function [66].

Recently, a fast functional PAM system was developed for high-resolution and high-speed imaging of the mouse brain [67, 68]. By employing a water-immersed microelectromechanical system (MEMS) scanning mirror (Fig. 18a), this PAM system achieved a 2D frame rate of 400 Hz over a 3 mm scanning range, with a 3 μ m lateral resolution and a 15 μ m axial resolution. Using a single-wavelength

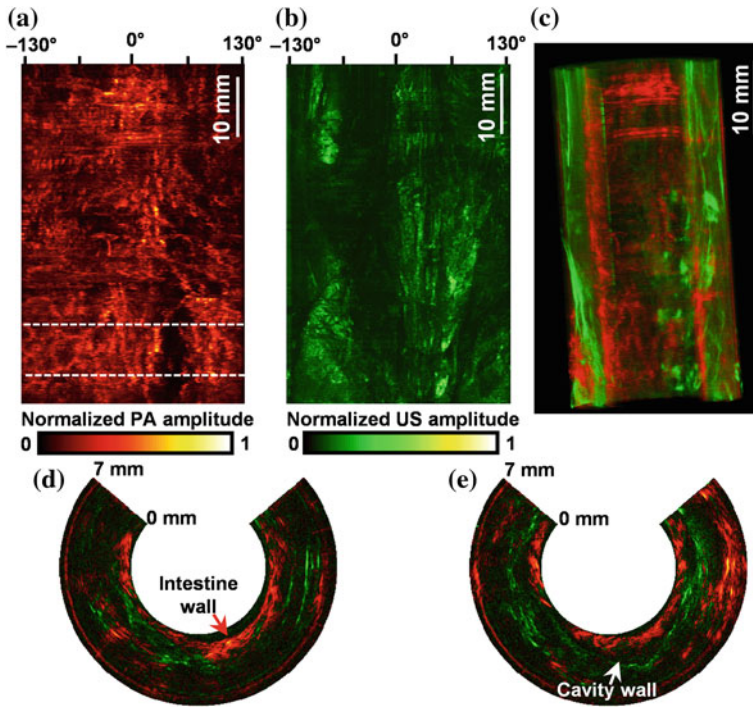


Fig. 17 Photoacoustic (a) and ultrasound (b) endoscopy images of a rabbit colorectum in vivo. c Co-registered PA and US image. d and e Representative combined PA and US B-scan images along the dashed line in (a) (Figure reprinted with permission from [64])

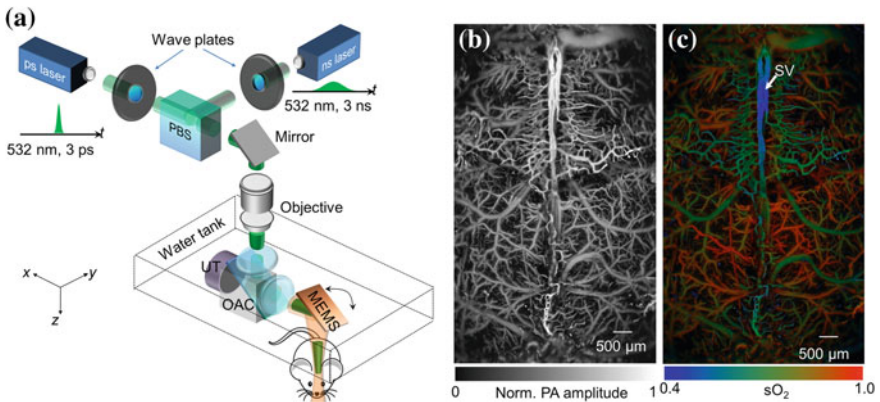


Fig. 18 Fast functional PAM of the mouse brain. a Schematic of the PAM system. OAC optical-acoustic coupler; PBS polarizing beam splitter; UT ultrasonic transducer. Representative structural (b) and functional (c) PA images of the mouse brain. SV skull vessel (Figure reprinted with permission from [68])

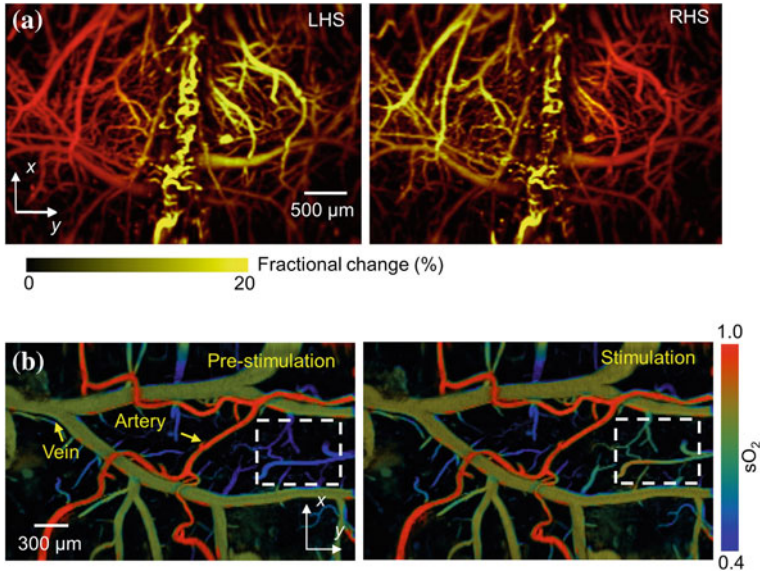


Fig. 19 Fast functional PAM of brain response in mice to electrical stimulations of the hindlimbs. **a** PA amplitude changes (shown in *yellow*) during left hindlimb stimulation (LHS) and right hindlimb stimulation (RHS). **b** sO₂ changes (marked by the *dashed boxes*) before and during stimulations of the left hindlimb (Figure reprinted with permission from [68])

pulse-width-based method, blood oxygenation could be imaged at a 1D rate of 100 kHz with two laser beams of different pulse widths (Fig. 18a, b shows a typical PA image of the mouse brain with intact skull, where the cortex vasculature can be observed in detail. The corresponding oxygen saturation of hemoglobin (sO₂) map is shown in Fig. 18c. It is worth mentioning that, because of the high imaging speed of this PAM system, only 40 s were required to acquire an sO₂ map of this large field of view.

To further demonstrate the capability of this PAM in high speed functional imaging, the authors studied mouse cortical hemodynamic responses to electrical stimulations of the hindlimbs. As shown in Fig. 19a, the PA signals in the corresponding regions increased upon stimulation. In addition, sO₂ levels increased in the veins and deep capillary beds, as shown in Fig. 19b. However, there was no sO₂ change in the arteries, which is consistent with the fact that arterial blood had not reached capillaries for oxygen exchange and thus retained a high oxygenation level.

Because this is an OR-PAM system, it works only in the ballistic regime. The mouse skull is relatively transparent, so only the scalp needs to be removed to achieve brain imaging. However, both the skull and scalp are thick in humans, so we cannot directly translate this high-resolution technology to image human brains. Nevertheless, because this system is fast (~ 400 Hz 2D frame rate), it has high potential for such applications, as providing anatomic vasculature images for surgical guidance and monitoring hemodynamic changes for operational feedback in real time.

4 Conclusions and Future Outlook

In summary, PAM has many translational applications, ranging from microvasculature disease detection to skin lesion (i.e., melanoma) identification and measurement. In this chapter, we have first introduced the basic principles and major implementations of PAM. The state-of-the-art applications, such as diabetes microvasculature detection and melanoma depth quantification have been discussed. Potential applications not discussed in this chapter include detecting oral lesion, and breast and urogenital cancers.

The metabolic rate of oxygen (MRO_2) is a crucial parameter for quantitatively screening and treating metabolic diseases, such as cancer [69]. To measure MRO_2 , three parameters—the cross sections of blood vessels, the oxygen saturation of hemoglobin, and blood flow velocity—need to be accurately detected. As discussed above, OR-PAM can accurately measure all of these parameters. So far, *in vivo* MRO_2 measurement has been achieved in the mouse model, but not yet in humans. One of the greatest challenges is accurately measuring blood flow velocity in humans *in vivo*. Because vessels are often deeply embedded below the skin in humans, only AR-PAM can directly measure them with high contrast. However, because of the relatively large voxel size in AR-PAM measurements, the requirement of signal heterogeneity cannot be fulfilled [60]. In the end, AR-PAM cannot directly measure blood flow velocity. However, with the help of high-intensity focused ultrasonic transducer (HIFU) heating [70], deep flow velocity has recently been successfully detected, which enables potential MRO_2 measurement in humans by PAM. Another possible way to detect blood flow velocity in humans is to use ultrasound, which has been widely used in clinics. Thus, a hybrid PAM and ultrasound system provides new possibilities for MRO_2 measurements in humans [71].

Temperature is another crucial physiological parameter, whose accurate measurement is essential for thermal therapy. Based on different mechanisms, current methods for measuring temperature by PAM can be divided into temperature dependent photoacoustic response methods [72–75], fluorescence-assisted photoacoustic-thermometry [76], and the two-state ratiometric method [77]. All these methods have shown high sensitivity in temperature measurements. However, because of the requirements for calibration, none of them have yet been applied *in vivo*, and calibration-free measurement remains to be developed.

Considering that OR-PAM can work only in the ballistic regime, we believe that two directions towards translational applications are feasible. One direction is to deepen the ballistic regime by using long wavelength light [78]. Because longer wavelength photons suffer less scattering, NIR light provides deeper penetration than visible light. Wave-front engineering can also be employed to focus light at depths [79–84]. By adjusting the incident light wave front or encoding the light at a targeted location, fine optical focus can be achieved inside the scattering medium. The second direction is tissue or cell imaging. Based on endogenous contrast, multi-wavelength OR-PAM can potentially be used for label-free histology [9, 12] and cytometry [85, 86] in addition to functional imaging.

Although AR-PAM has already shown its deep imaging capability, it cannot provide functional information, such as the sO_2 , as accurately as OR-PAM. Because wavelength-dependent attenuation differs more at greater imaging depths, multi-wavelength-based sO_2 measurement is less accurate in AR-PAM than in OR-PAM. Recently, a single-wavelength-based method for sO_2 measurement was proposed [68], which could potentially be used in AR-PAM to provide more accurate sO_2 results. Consequently, AR-PAM holds promise for translational applicability, such as for tumor screening and blood disorder diagnosis.

Acknowledgments The authors would like to thank Profs. James Ballard and Sandra Matteucci for manuscript editing. This work was supported in part by National Institutes of Health grants DP1 EB016986 (NIH Director's Pioneer Award), R01 CA186567 (NIH Director's Transformative Research Award), U01 NS090579 (BRAIN Initiative), R01 EB016963, R01 EB010049, R01 CA157277, and R01 CA159959 as well as National Science Foundation grant 1255930. L.W. has a financial interest in Microphotoacoustics, Inc. and Endra, Inc., which, however, did not support this work.

References

1. L.V. Wang, H. Wu, *Biomedical Optics: Principles and Imaging* (Wiley, Hoboken, 2007)
2. A.T. Eggebrecht, S.L. Ferradal, A. Robichaux-Viehoever, M.S. Hassanpour, H. Dehghani, A.Z. Snyder, T. Hershey, J.P. Culver, Mapping distributed brain function and networks with diffuse optical tomography. *Nat. Photonics* **8**, 448–454 (2014)
3. L.H.V. Wang, S. Hu, Photoacoustic tomography in vivo imaging from organelles to organs. *Science* **335**, 1458–1462 (2012)
4. L.V. Wang, Multiscale photoacoustic microscopy and computed tomography. *Nat. Photonics* **3**, 503–509 (2009)
5. H.F. Zhang, K. Maslov, G. Stoica, L.H.V. Wang, Functional photoacoustic microscopy for high-resolution and noninvasive in vivo imaging. *Nat. Biotechnol.* **24**, 848–851 (2006)
6. X.D. Wang, Y.J. Pang, G. Ku, X.Y. Xie, G. Stoica, L.H.V. Wang, Noninvasive laser-induced photoacoustic tomography for structural and functional in vivo imaging of the brain. *Nat. Biotechnol.* **21**, 803–806 (2003)
7. S. Hu, L.H.V. Wang, Optical-resolution photoacoustic microscopy: auscultation of biological systems at the cellular level. *Biophys. J.* **105**, 841–847 (2013)
8. C. Zhang, Y.J. Cheng, J.J. Chen, S. Wickline, L.H.V. Wang, Label-free photoacoustic microscopy of myocardial sheet architecture. *J. Biomed. Opt.* **17** (2012)
9. D.K. Yao, K. Maslov, K.K. Shung, Q.F. Zhou, L.V. Wang, In vivo label-free photoacoustic microscopy of cell nuclei by excitation of DNA and RNA. *Opt. Lett.* **35**, 4139–4141 (2010)
10. Z. Xu, C.H. Li, L.V. Wang, Photoacoustic tomography of water in phantoms and tissue. *J. Biomed. Opt.* **15** (2010)
11. H.W. Wang, N. Chai, P. Wang, S. Hu, W. Dou, D. Umulis, L.H.V. Wang, M. Sturek, R. Lucht, J.X. Cheng, Label-free bond-selective imaging by listening to vibrationally excited molecules. *Phys. Rev. Lett.* **106** (2011)
12. C. Zhang, Y.S. Zhang, D.K. Yao, Y.N. Xia, L.H.V. Wang, Label-free photoacoustic microscopy of cytochromes. *J. Biomed. Opt.* **18** (2013)
13. Y. Zhou, C. Zhang, D.K. Yao, L.H.V. Wang, Photoacoustic microscopy of bilirubin in tissue phantoms. *J. Biomed. Opt.* **17** (2012)

14. Y. Wang, K. Maslov, Y. Zhang, S. Hu, L.M. Yang, Y.N. Xia, J.A. Liu, L.H.V. Wang, Fiber-laser-based photoacoustic microscopy and melanoma cell detection. *J. Biomed. Opt.* **16** (2011)
15. Y. Zhou, G. Li, L. Zhu, C. Li, L.A. Cornelius, L.V. Wang, Handheld photoacoustic probe to detect both melanoma depth and volume at high speed in vivo. *J. Biophotonics.* **1** (2015)
16. M. Tang, Y. Zhou, R. Zhang, L.V. Wang, Noninvasive photoacoustic microscopy of methemoglobin in vivo. *J. Biomed. Opt.* **20**, 036007 (2015)
17. C. Zhang, K. Maslov, L.H.V. Wang, Subwavelength-resolution label-free photoacoustic microscopy of optical absorption in vivo. *Opt. Lett.* **35**, 3195–3197 (2010)
18. A. Danielli, K. Maslov, A. Garcia-Uribe, A.M. Winkler, C.Y. Li, L.D. Wang, Y. Chen, G.W. Dorn, L.V. Wang, Label-free photoacoustic nanoscopy. *J. Biomed. Opt.* **19** (2014)
19. S. Hu, K. Maslov, L.V. Wang, Second-generation optical-resolution photoacoustic microscopy with improved sensitivity and speed. *Opt. Lett.* **36**, 1134–1136 (2011)
20. R.A. Kruger, C.M. Kuzmiak, R.B. Lam, D.R. Reinecke, S.R. Del Rio, D. Steed, Dedicated 3D photoacoustic breast imaging. *Med. Phys.* **40** (2013)
21. C.P. Favazza, O. Jassim, L.A. Cornelius, L.H.V. Wang, In vivo photoacoustic microscopy of human cutaneous microvasculature and a nevus. *J. Biomed. Opt.* **16** (2011)
22. H.F. Zhang, K. Maslov, G. Stoica, L.H.V. Wang, Imaging acute thermal burns by photoacoustic microscopy. *J. Biomed. Opt.* **11** (2006)
23. W. Song, Q. Wei, L. Feng, V. Sarthy, S.L. Jiao, X.R. Liu, H.F. Zhang, Multimodal photoacoustic ophthalmoscopy in mouse. *J. Biophotonics* **6**, 505–512 (2013)
24. Y. Zhou, W. Xing, K.I. Maslov, L.A. Cornelius, L.V. Wang, Handheld photoacoustic microscopy to detect melanoma depth in vivo. *Opt. Lett.* **39**, 4731–4734 (2014)
25. J.M. Yang, C. Favazza, R.M. Chen, J.J. Yao, X. Cai, K. Maslov, Q.F. Zhou, K.K. Shung, L.H.V. Wang, Simultaneous functional photoacoustic and ultrasonic endoscopy of internal organs in vivo. *Nat. Med.* **18**, 1297 (2012)
26. K. Maslov, H.F. Zhang, S. Hu, L.V. Wang, Optical-resolution photoacoustic microscopy for in vivo imaging of single capillaries. *Opt. Lett.* **33**, 929–931 (2008)
27. K. Maslov, G. Stoica, L.H.V. Wang, In vivo dark-field reflection-mode photoacoustic microscopy. *Opt. Lett.* **30**, 625–627 (2005)
28. K. Maslov, L.V. Wang, Photoacoustic imaging of biological tissue with intensity-modulated continuous-wave laser. *J. Biomed. Opt.* **13** (2008)
29. C. Zhang, Y. Zhou, C.Y. Li, L.H.V. Wang, Slow-sound photoacoustic microscopy. *Appl. Phys. Lett.* **102** (2013)
30. C. Zhang, K. Maslov, J.J. Yao, L.H.V. Wang, In vivo photoacoustic microscopy with 7.6 μm axial resolution using a commercial 125-MHz ultrasonic transducer. *J. Biomed. Opt.* **17** (2012)
31. E.W. Stein, K. Maslov, L.H.V. Wang, Noninvasive, in vivo imaging of the mouse brain using photoacoustic microscopy. *J. Appl. Phys.* **105** (2009)
32. J.Y. Liang, Y. Zhou, A.W. Winkler, L.D. Wang, K.I. Maslov, C.Y. Li, L.H.V. Wang, Random-access optical-resolution photoacoustic microscopy using a digital micromirror device. *Opt. Lett.* **38**, 2683–2686 (2013)
33. Y. Zhou, J.Y. Liang, K.I. Maslov, L.H.V. Wang, Calibration-free in vivo transverse blood flowmetry based on cross correlation of slow time profiles from photoacoustic microscopy. *Opt. Lett.* **38**, 3882–3885 (2013)
34. J.Y. Liang, Y. Zhou, K.I. Maslov, L.H.V. Wang, Cross-correlation-based transverse flow measurements using optical resolution photoacoustic microscopy with a digital micromirror device. *J. Biomed. Opt.* **18** (2013)
35. J.J. Yao, L.H.V. Wang, Transverse flow imaging based on photoacoustic Doppler bandwidth broadening. *J. Biomed. Opt.* **15** (2010)
36. J.J. Yao, K.I. Maslov, Y.F. Shi, L.A. Taber, L.H.V. Wang, In vivo photoacoustic imaging of transverse blood flow by using Doppler broadening of bandwidth. *Opt. Lett.* **35**, 1419–1421 (2010)
37. Y. Zhou, J.J. Yao, L.H.V. Wang, Optical clearing-aided photoacoustic microscopy with enhanced resolution and imaging depth. *Opt. Lett.* **38**, 2592–2595 (2013)

38. Y. Liu, C. Zhang, L.H.V. Wang, Effects of light scattering on optical-resolution photoacoustic microscopy. *J. Biomed. Opt.* **17** (2012)
39. G. Ku, L.H.V. Wang, Deeply penetrating photoacoustic tomography in biological tissues enhanced with an optical contrast agent. *Opt. Lett.* **30**, 507–509 (2005)
40. T. Ida, Y. Kawaguchi, S. Kawauchi, K. Iwaya, H. Tsuda, D. Saitoh, S. Sato, T. Iwai, Real-time photoacoustic imaging system for burn diagnosis. *J. Biomed. Opt.* **19** (2014)
41. K. Aizawa, S. Sato, D. Saitoh, H. Ashida, M. Obara, Photoacoustic monitoring of burn healing process in rats. *J. Biomed. Opt.* **13** (2008)
42. R. Kragelj, T. Jarm, T. Erjavec, M. Presern-Strukelj, D. Miklavcic, Parameters of postocclusive reactive hyperemia measured by near infrared spectroscopy in patients with peripheral vascular disease and in healthy volunteers. *Ann. Biomed. Eng.* **29**, 311–320 (2001)
43. G. Addor, A. Delachaux, B. Dischl, D. Hayoz, L. Liaudet, B. Waeber, F. Feihl, A comparative study of reactive hyperemia in human forearm skin and muscle. *Physiol. Res.* **57**, 685–692 (2008)
44. C.P. Favazza, L.A. Cornelius, L.H.V. Wang, In vivo functional photoacoustic microscopy of cutaneous microvasculature in human skin. *J. Biomed. Opt.* **16** (2011)
45. F.F.M. de Mul, F. Morales, A.J. Smit, R. Graaff, A model for post-occlusive reactive hyperemia as measured with laser-Doppler perfusion monitoring. *IEEE T. Bio-Med. Eng.* **52**, 184–190 (2005)
46. D. Lepore, F. Molle, M.M. Pagliara, A. Baldascino, C. Angora, M. Sammartino, G.E. Quinn, Atlas of fluorescein angiographic findings in eyes undergoing laser for retinopathy of prematurity. *Ophthalmology* **118**, 168–175 (2011)
47. S. Makita, F. Jaillon, M. Yamanari, M. Miura, Y. Yasuno, Comprehensive in vivo micro-vascular imaging of the human eye by dual-beam-scan Doppler optical coherence angiography. *Opt. Express* **19**, 1271–1283 (2011)
48. A. de la Zerda, Y.M. Paulus, R. Teed, S. Bodapati, Y. Dollberg, B.T. Khuri-Yakub, M.S. Blumenkranz, D.M. Moshfeghi, S.S. Gambhir, Photoacoustic ocular imaging. *Opt. Lett.* **35**, 270–272 (2010)
49. S.L. Jiao, M.S. Jiang, J.M. Hu, A. Fawzi, Q.F. Zhou, K.K. Shung, C.A. Puliafito, H.F. Zhang, Photoacoustic ophthalmoscopy for in vivo retinal imaging. *Opt. Express* **18**, 3967–3972 (2010)
50. S. Hu, B. Rao, K. Maslov, L.V. Wang, Label-free photoacoustic ophthalmic angiography. *Opt. Lett.* **35**, 1–3 (2010)
51. N. Wu, S.Q. Ye, Q.S. Ren, C.H. Li, High-resolution dual-modality photoacoustic ocular imaging. *Opt. Lett.* **39**, 2451–2454 (2014)
52. W. Song, Q. Wei, T. Liu, D. Kuai, J.M. Burke, S.L. Jiao, H.F. Zhang, Integrating photoacoustic ophthalmoscopy with scanning laser ophthalmoscopy, optical coherence tomography, and fluorescein angiography for a multimodal retinal imaging platform. *J. Biomed. Opt.* **17** (2012)
53. Y.K. Shi, F.B. Hu, The global implications of diabetes and cancer. *Lancet* **383**, 1947–1948 (2014)
54. N. Sarwar, P. Gao, S.R.K. Seshasai, R. Gobin, S. Kaptoge, E. Di Angelantonio, E. Ingelsson, D.A. Lawlor, E. Selvin, M. Stampfer, C.D.A. Stehouwer, S. Lewington, L. Pennells, A. Thompson, N. Sattar, I.R. White, K.K. Ray, J. Danesh, E.R.F. Collabora, Diabetes mellitus, fasting blood glucose concentration, and risk of vascular disease: a collaborative meta-analysis of 102 prospective studies. *Lancet* **375**, 2215–2222 (2010)
55. P.T. O’Gara, F.G. Kushner, D.D. Ascheim, D.E. Casey, M.K. Chung, J.A. de Lemos, S.M. Ettinger, J.C. Fang, F.M. Fesmire, B.A. Franklin, C.B. Granger, H.M. Krumholz, J.A. Linderbaum, D.A. Morrow, L.K. Newby, J.P. Ornato, N. Ou, M.J. Radford, J.E. Tamis-Holland, C.L. Tommaso, C.M. Tracy, Y.J. Woo, D.X. Zhao, W.C. Members, 2013 ACCF/AHA guideline for the management of ST-elevation myocardial infarction a report of the american college of cardiology foundation/american heart association task force on practice guidelines. *Circulation*. **127**, E362 (2013)

56. A. Krumholz, L.D. Wang, J.J. Yao, L.H.V. Wang, Functional photoacoustic microscopy of diabetic vasculature. *J. Biomed. Opt.* **17** (2012)
57. L. Parkitny, J.H. McAuley, F. Di Pietro, T.R. Stanton, N.E. O'Connell, J. Marinus, J.J. van Hilten, G.L. Moseley, Inflammation in complex regional pain syndrome a systematic review and meta-analysis. *Neurology.* **80**, 106–117 (2013)
58. M. Schurmann, J. Zaspel, G. Gradl, A. Wipfel, F. Christ, Assessment of the peripheral microcirculation using computer-assisted venous congestion plethysmography in post-traumatic complex regional pain syndrome type I. *J. Vasc. Res.* **38**, 453–461 (2001)
59. Y. Zhou, X.B. Yi, W.X. Xing, S. Hu, K.I. Maslov, L.H.V. Wang, Microcirculatory changes identified by photoacoustic microscopy in patients with complex regional pain syndrome type I after stellate ganglion blocks. *J. Biomed. Opt.* **19** (2014)
60. Y. Zhou, J. Yao, K.I. Maslov, L.V. Wang, Calibration-free absolute quantification of particle concentration by statistical analyses of photoacoustic signals in vivo. *J. Biomed. Opt.* **19**, 37001 (2014)
61. A.F. Jerant, J.T. Johnson, C.D. Sheridan, T.J. Caffrey, Early detection and treatment of skin cancer. *American family physician.* **62**, 357–368, 375–376, 381–382 (2000)
62. K.M. Rubin, Melanoma staging: a review of the revised american joint committee on cancer guidelines. *J. Dermatol. Nurses Assoc.* **2**, 6 (2010)
63. J.M. Yang, C.Y. Li, R.M. Chen, Q.F. Zhou, K.K. Shung, L.V. Wang, Catheter-based photoacoustic endoscope. *J. Biomed. Opt.* **19** (2014)
64. C.Y. Li, J.M. Yang, R.M. Chen, C.H. Yeh, L.R. Zhu, K. Maslov, Q.F. Zhou, K.K. Shung, L.H.V. Wang, Urogenital photoacoustic endoscope. *Opt. Lett.* **39**, 1473–1476 (2014)
65. J.M. Yang, R.M. Chen, C. Favazza, J.J. Yao, C.Y. Li, Z.L. Hu, Q.F. Zhou, K.K. Shung, L.V. Wang, A 2.5-mm diameter probe for photoacoustic and ultrasonic endoscopy. *Opt. Express* **20**, 23944–23953 (2012)
66. M.E. Raichle, A paradigm shift in functional brain imaging. *J. Neurosci.* **29**, 12729–12734 (2009)
67. J.J. Yao, C.H. Huang, L.D. Wang, J.M. Yang, L. Gao, K.I. Maslov, J. Zou, L.H.V. Wang, Wide-field fast-scanning photoacoustic microscopy based on a water-immersible MEMS scanning mirror. *J. Biomed. Opt.* **17** (2012)
68. J.J. Yao, L.D. Wang, J.M. Yang, K.I. Maslov, T.W. Wong, L. Li, C.H. Huang, J. Zou, L.H.V. Wang, High-speed label-free functional photoacoustic microscopy of mouse brain in action. *Nat. Methods* (2015)
69. J.J. Yao, K.I. Maslov, Y. Zhang, Y.N. Xia, L.V. Wang, Label-free oxygen-metabolic photoacoustic microscopy in vivo. *J. Biomed. Opt.* **16** (2011)
70. L.D. Wang, J. Xia, J.J. Yao, K.I. Maslov, L.H.V. Wang, Ultrasonically encoded photoacoustic flowgraphy in biological tissue. *Phys. Rev. Lett.* **111** (2013)
71. Y. Jiang, A. Forbrich, T. Harrison, R.J. Zemp, Blood oxygen flux estimation with a combined photoacoustic and high-frequency ultrasound microscopy system: a phantom study. *J. Biomed. Opt.* **17** (2012)
72. E.V. Petrova, A.A. Oraevsky, S.A. Ermilov, Red blood cell as a universal optoacoustic sensor for non-invasive temperature monitoring. *Appl. Phys. Lett.* **105** (2014)
73. H.X. Ke, S. Tai, L.H.V. Wang, Photoacoustic thermography of tissue. *J. Biomed. Opt.* **19** (2014)
74. M. Pramanik, L.V. Wang, Thermoacoustic and photoacoustic sensing of temperature. *J. Biomed. Opt.* **14** (2009)
75. L. Gao, L.D. Wang, C.Y. Li, Y. Liu, H.X. Ke, C. Zhang, L.H.V. Wang, Single-cell photoacoustic thermometry. *J. Biomed. Opt.* **18** (2013)
76. L. Gao, C. Zhang, C.Y. Li, L.H.V. Wang, Intracellular temperature mapping with fluorescence-assisted photoacoustic-thermometry. *Appl. Phys. Lett.* **102** (2013)
77. J.J. Yao, H.X. Ke, S. Tai, Y. Zhou, L.H.V. Wang, Absolute photoacoustic thermometry in deep tissue. *Opt. Lett.* **38**, 5228–5231 (2013)
78. P.F. Hai, J.J. Yao, K.I. Maslov, Y. Zhou, L.H.V. Wang, Near-infrared optical-resolution photoacoustic microscopy. *Opt. Lett.* **39**, 5192–5195 (2014)

79. X.A. Xu, H.L. Liu, L.V. Wang, Time-reversed ultrasonically encoded optical focusing into scattering media. *Nat. Photonics* **5**, 154–157 (2011)
80. T. Chaigne, O. Katz, A.C. Boccara, M. Fink, E. Bossy, S. Gigan, Controlling light in scattering media non-invasively using the photoacoustic transmission matrix. *Nat. Photonics* **8**, 59–65 (2014)
81. A.P. Mosk, A. Lagendijk, G. Lerosey, M. Fink, Controlling waves in space and time for imaging and focusing in complex media. *Nat. Photonics* **6**, 283–292 (2012)
82. Y. Liu, P.X. Lai, C. Ma, X. Xu, A.A. Grabar, L.V. Wang, Optical focusing deep inside dynamic scattering media with near-infrared time-reversed ultrasonically encoded (TRUE) light. *Nat. Commun.* **6** (2015)
83. P.X. Lai, L.D. Wang, J.W. Tay, L.H.V. Wang, Photoacoustically guided wavefront shaping for enhanced optical focusing in scattering media. *Nat. Photonics* **9**, 126–132 (2015)
84. C. Ma, X. Xu, Y. Liu, L.V. Wang, Time-reversed adapted-perturbation (TRAP) optical focusing onto dynamic objects inside scattering media. *Nat. Photon.* **8**, 931–936 (2014)
85. E.I. Galanzha, E.V. Shashkov, P.M. Spring, J.Y. Suen, V.P. Zharov, In vivo, noninvasive, label-free detection and eradication of circulating metastatic melanoma cells using two-color photoacoustic flow cytometry with a diode laser. *Cancer Res.* **69**, 7926–7934 (2009)
86. E.I. Galanzha, E.V. Shashkov, T. Kelly, J.W. Kim, L.L. Yang, V.P. Zharov, In vivo magnetic enrichment and multiplex photoacoustic detection of circulating tumour cells. *Nat. Nanotechnol.* **4**, 855–860 (2009)